On the impact of true polar wander on heat flux patterns at the core-mantle boundary

Thomas Frasson[1], Stéphane Labrosse[2], Henri-Claude Nataf[1], Nicolas Coltice[3], and Nicolas Flament[4]

[1]Univ. Grenoble Alpes, Univ. Savoie Mont Blanc, CNRS, IRD, Univ. Gustave Eiffel, ISTerre, 38000 Grenoble, France
[2]ENS de Lyon, Lyon, France
[3]ENS, Paris, France
[4]School of Earth and Environmental Sciences, Univ. of Wollongong, Northfields Avenue, NSW 2522, Australia

Correspondence: Thomas Frasson (thomas.frasson@univ-grenoble-alpes.fr)

Abstract. Heat flux across the core-mantle boundary (CMB) is an important variable of Earth's thermal evolution and dynamics. Seismic tomography provides access to seismic heterogeneities in the lower mantle, which can be related to present-day thermal heterogeneities. Alternatively, mantle convection models can be used to either infer past CMB heat flux or to produce statistically realistic CMB heat flux patterns in self-consistent models. Mantle dynamics modifies the inertia tensor of the Earth, which implies a rotation of the Earth with respect to its spin axis, a phenomenon called true polar wander (TPW). This rotation must be taken into account to link the dynamics of the mantle to the dynamics of the core. In this study, we use two recently published mantle convection models to explore the impact of TPW on the CMB heat flux over long timescales ($\sim$ 1 Gyr). One of the mantle convection models is driven by a plate reconstruction, while the other self-consistently produces a plate-like behavior. We compute the geoid in both models to correct for TPW. In the plate-driven model, we compute a total geoid and a geoid in which lateral variations of viscosity and temperature are suppressed above 350 km depth. We show that TPW plays an important role in redistributing the CMB heat flux, notably at short time scales ($\leq$ 10 Myr). Those rapid variations modify the latitudinal distribution of the CMB heat flux, which is known to affect the stability of the magnetic dipole in geodynamo simulations. A principal component analysis (PCA) is computed to obtain the dominant CMB heat flux pattern in the different cases. These heat flux patterns can be used as boundary conditions for geodynamo models as representative of the mantle convection cases studied here. We note that the geoids produced by the two models are widely different from each other and from the observed present-day geoid. Work thus still needs to be done to improve the computation of the geoid in mantle convection models related to plate-tectonics.

1 Introduction

Temperature heterogeneities in the lower mantle imposes an heterogeneous heat flux at the top of the core, across the core-mantle boundary (CMB). This CMB heat flux is an important variable of Earth's thermal evolution and dynamics, especially regarding core convection and the geodynamo. The mean CMB heat flux controls the core cooling rate, which determines the power available for the geodynamo. Both the CMB heat flux mean value and lateral variations affect dynamo behavior in numerical simulations, with strong effects on magnetic reversal frequency and on the angle between spin and magnetic dipole

axes (Glatzmaier et al., 1999; Kutzner and Christensen, 2004; Olson et al., 2010). Large heat flux heterogeneities can even
25   prevent dynamo action (Olson and Christensen, 2002). It is therefore important to evaluate what could be the evolution of the
CMB heat flux on geologic timescales, in order to assess consequences for the geodynamo.

Because viscosities are much larger in Earth's mantle than in Earth's outer core, the CMB is an isothermal boundary for the
mantle, while the core sees the CMB as an imposed laterally varying heat flux. This heat flux changes on mantle convection
timescales, which are much larger than core dynamics timescales. The level of knowledge of the CMB heat flux, and notably its
30   spatial distribution, depends on our understanding of lower mantle structure and dynamics. Seismic tomography offers a view
of the lowermost mantle, revealing more and more complex structures (e.g. Dziewonski et al., 1977; Lay and Helmberger, 1983;
Garnero and Helmberger, 1995; Su and Dziewonski, 1997; Durand et al., 2017) (see Ritsema and Lekić, 2020, for a review).
Around the equator, two antipodal large low velocity provinces (LLVPs) are particularly conspicuous, and are interpreted as
thermochemical piles (Garnero and McNamara, 2008). They form a characteristic structure dominated by spherical harmonics
35   degree 2. LLVPs are correlated with the degree 2 geoid, with positive geoid anomalies observed over each LLVP (Dziewonski
et al., 1977). At scales too small to be resolved in global tomographic models, ultra low velocity zones (ULVZ) have also been
observed using dedicated approaches (e.g. Garnero and Helmberger, 1995; Rost et al., 2005). Despite these improvements, it is
still difficult to have a clear view of the CMB heat flux pattern. Thermal and chemical effects are notably difficult to distinguish
in tomographic models (Trampert, 2004; Mosca et al., 2012), which only provides a present-day snapshot of Earth's history.

40   Records of hotspots's eruption locations suggest that LLVPs could have remained fixed for the past 300 Myr at least (Burke
et al., 2008), providing a stable large-scale heat flux pattern through time. This view of stable LLVPs has however been
challenged by recent seismic tomography models (Davaille and Romanowicz, 2020) and mantle flow reconstructions (Flament
et al., 2022). Past CMB heat flux estimates have been obtained from reconstructions of mantle flow driven by observed plate
motions for the past 450 Myr (Zhang and Zhong, 2011; Olson et al., 2015), and more recently for the past 1 Gyr (Flament et al.,
45   2022). These models show that the CMB heat flux pattern is governed by plate motion through subducted slabs, which cool the
lower mantle. Large lowermost mantle chemical piles reduce heat transfer, thereby increasing overall lateral heterogeneities of
CMB heat flux. CMB heat flux reconstructions can thus be used to constrain core evolution and magnetic field generation. Olson
et al. (2015) use these models to drive a thermal evolution model of the core, while Zhang and Zhong (2011) found equatorial
heat flux minima around 170 Myr and 100 Myr ago, which coincide with Kiaman and Cretaceous magnetic superchrons,
50   respectively.

These models are useful to explore the past of mantle convection. They are however limited by the accuracy of plate recon-
structions, which remain poorly constrained before the assembly of Pangea (Müller et al., 2022). Alternatively, CMB heat flux
estimates can be obtained from self-consistent models, without prescribed surface velocities (Liu and Zhong, 2015; Coltice
et al., 2019). This approach is less "Earth-like" than models with prescribed plate motion in that it does not aim at reproducing
55   actual Earth's past. However, it makes it possible to obtain statistically realistic information on mantle convection depending
on input parameters. Using this kind of model, Nakagawa and Tackley (2008) notably showed that lateral variations in the
CMB heat flux could be as large as the mean CMB heat flux.

This work aims at describing CMB heat flux produced by two up-to-date mantle convection models. One is driven by a reconstructed surface plates, while the other one is entirely self-consistent and free to evolve. For each model, we notably provide representative CMB heat flux maps that can be used in geodynamo simulations. These maps are obtained using a principal component analysis (PCA), which brings out dominant CMB heat flux patterns.

Earth's spin plays a crucial role in core dynamics. If we are to explore the impact of realistic CMB heat flux patterns on the geodynamo, it is essential that these patterns be produced in a reference frame that preserves the spin axis. Mantle convection simulations do not depend on the position of Earth's spin axis since rotational forces are negligible in the mantle, and surface and CMB boundary conditions are not affected by a global rotation of the mantle with respect to its spin axis. However, mass redistribution and boundary topographies caused by convection modify the moments of inertia of the mantle (Munk and MacDonald, 1960; Phillips et al., 2009), which can be obtained from the degree 2 coefficients of the geoid (MacCullagh, 1845; Schaber et al., 2009). The mantle therefore rotates in order to keep its axis of greatest inertia along spin axis (Goldreich and Toomre, 1969). This is called true polar wander (TPW). TPW emerging from mantle convection models has been studied to retrieve the past track of the spin axis (Steinberger and O'Connell, 1997; Schaber et al., 2009), or to investigate the link between supercontinents and TPW in freely-evolving convection models (Zhong et al., 2007; Phillips et al., 2009). In these models, plate tectonics is either prescribed or approximated. Here, we extract CMB heat flux and geoid from two different mantle convection models, compute TPW from the degree two of the geoid, and rotate the simulation frame accordingly to position CMB heat flux maps in the reference frame relevant to core dynamics.

Section 2 describes the methods used for the successive steps of the analysis. Results are presented in Sect. 3 and discussed in Sect. 4. We conclude in Sect. 5.

2 Methods

2.1 3D mantle convection models

Our study rests upon an analysis of two published 3D mantle convection simulations. Both models simulate mantle convection in a 3D spherical shell including tectonic plates at the surface, and chemical piles at the bottom. They however differ in the way plate-tectonics is handled. The first model (similar to case NNR of Müller et al. (2022)), named MF in the following, is driven by plates with structure and kinematics derived from geological observations. This model thus aims to reproduce the actual history of Earth's mantle convection, using constraints from surface kinematics and the position of subduction zones. The second model (Coltice et al., 2019), named MC in the following, produces a plate-like behavior without imposing any surface kinematics. Plate-like structures and subduction zones are obtained in a fully self-consistent way using a pseudo-plastic rheology and a strongly temperature-dependent viscosity. This model does not aim to reproduce the actual past or future history of mantle convection. Instead, it provides an alternative convection history with statistically realistic parameters. The following paragraphs describe the characteristics of those models relevant for this study.

2.1.1 MF model

90 Model MF was computed using the code CitcomS (Zhong et al., 2008; Bower et al., 2015). The model is driven at the surface by imposing plate velocities, the positions of subduction zones, and the age of the oceanic lithosphere. These constraints are taken from a no-net-rotation mantle reference frame based on the plate tectonics reconstruction of Merdith et al. (2021), which extends 1 Gyr in the past. The model is initialized at 1.25 Gyr ago (Ga) with a 250-Myr warm-up phase during which tectonic velocities, subduction zone positions and lithospheric ages are derived from the tectonic reconstruction at 1 Ga. The

95 initial condition at 1.25 Ga consisted of slabs inserted down to 1,000 km depth and of a 113 km-thick basal layer of material with excess density $\delta\rho_c/\rho_{100}$ = 1.7% compared to the ambient mantle where $\rho_{100} = 5546$ kg m^{-3} is the average density in the bottom 100 km of the mantle in the PREM model (Dziewonski and Anderson, 1981). After the warm-up phase, surface boundary conditions are updated in one-million-year increments with linear interpolation at each numerical time step. The model is similar to case NNR of Müller et al. (2022), with differences listed below. The Rayleigh number (based on the

100 thickness of the mantle) is equal to 10^8 with an internal heating rate of 30 TW. Phase changes are considered at depths of 410 km, 670 km and 2740 km, and assumed to occur over a 40 km depth-range. At 410 km depth, the density change is 3% of ambient mantle density and the Clapeyron slope is equal to 4 MPa K^{-1} (Billen, 2008, and references therein). At 670 km depth, the density change is 7% of ambient mantle density and the Clapeyron slope is -2 MPa K^{-1} (Billen, 2008, and references therein). At 2740 km depth, the density change is 1.1% of ambient mantle density and the Clapeyron slope is 12 MPa K^{-1}

105 (Nakagawa and Tackley, 2014).

This model predicts CMB heat flux based on a reconstruction of past positions of tectonic plates and associated mantle flow. The evolution of the thermochemical basal boundary layer is dictated by subducting slabs, which are introduced at the surface following the plate model. Heat flux patterns are thus directly related to the past 1 Gyr of mantle convection history, which depends on the plate tectonic reconstruction imposed as surface boundary condition. Whilst the past 200 Myr are

110 well constrained notably from magnetic anomalies and hotspot tracks preserved in the oceanic crust, plate motions are more uncertain for earlier geological times. Advantages of model MF are that it generally matches the present-day structure of the mantle (Flament et al., 2022; Müller et al., 2022), and is designed to reconstruct Earth's mantle convection based on available constraints.

2.1.2 MC model

115 Model MC reproduces in total 1131 Myr of mantle evolution using the code StagYY in a 3-D Yin-Yang geometry (Tackley, 2008). This model has been set up to reproduce Earth-like mantle convection features, with particular attention to plate-like behavior. Coltice et al. (2019) presented results from this model focusing on plate-tectonics. Here, we use the same model to study the CMB heat flux. At the base of the mantle, chemical piles are modeled as a material denser than the surrounding mantle. Continents are modeled as a compositionally distinct material that is less dense and more viscous than the ambient

120 mantle, with 200 km-thick interiors and 125 km-thick rims. The reference density ρ_0 and viscosity η_0 have dimensional values

4000 kg m^{-3} and 10^{22} Pa s, respectively. The negative compositional density anomaly inside continents is $\delta\rho_c = -225$ kg m^{-3}, and the compositional density excess in basal piles is $\delta\rho_p = 137$ kg m^{-3}.

The initial state of the simulation is an equilibrated mantle circulation obtained with two fixed antipodal 500 km-thick chemical piles around the equator, and fixed continents assembled in a Pangea-like supercontinent placed above the "Atlantic"

125 pile. At the start of the simulation, continents and piles are allowed to move freely. The relaxation to a new statistically steady state takes about 300 Myr. The first 300 Myr are thus not considered in the following analysis.

In contrast with model MF, plate kinematics are not imposed in this model. A plate-like behavior is self-consistently produced using a pseudo-plastic rheology and a temperature-dependent viscosity (Tackley, 2000a, b). An uppermost 14 km-thick weak layer in oceanic regions makes it possible to obtain asymmetric subduction zones (Crameri et al., 2012). Model MC reproduces

130 a statistically realistic mantle convection that fits the observations of global features (plate dimensions and velocities, surface heat flux, hypsometry, plume buoyancy flux) as well as local features (continental breakup, rifting, back-arc extension, mantle plumes) as shown in Coltice et al. (2019). The extreme temperature-dependence of viscosity in the model gives rise to plumes that display kinematic, thermal and buoyancy properties similar to Earth's plumes (Arnould et al., 2020). Because plumes carry information from the CMB, these properties of the model are fundamental for our study.

135 Regarding the objective of this work, the main advantages of model MC are the Earth-likeness of surface processes and its long time evolution. It captures the effect of realistic plate tectonics on a CMB heat flux that varies in space and time over nearly 1 Gyr. Model MC notably contains a complete cycle of breakup and assembly of a super-continent, which is thought to modulate CMB heat flux (Olson et al., 2013; Amit et al., 2015). The similarity between model MC and the Earth at the bottom of the mantle is less certain. Nevertheless, the presence of chemical piles allows for strong, large-scale temperature

140 heterogeneities, as revealed by seismic tomography (Trampert, 2004; Mosca et al., 2012).

2.2 Geoid

TPW is controlled by the change in the Earth's moment of inertia around its spin axis. The moment of inertia is obtained from the degree 2 components of the geoid, which we thus need to compute for our mantle flow models. The geoid is the equipotential surface of gravity measured or computed around a reference level, sea level for the Earth, top of the model for

145 simulations. It can be computed by integration of lateral density variations across the mantle model. Additional contributions arise from lateral mass heterogeneities produced by deflections of interfaces, surface and CMB in particular. These deflections are not explicit in models (which assume spherical boundaries), but can be computed from element τ_{zz} of stress tensor $\boldsymbol{\tau}$ at interfaces, where z is the vertical coordinate. Geoid computation is an intrinsic capacity of both codes CitcomS and StagYY. It follows Zhang and Christensen (1993), and is implemented as in Zhong et al. (2008). Interface topographies and density

150 heterogeneities are projected on spherical harmonics Y_l^m. Surface geoid and interface topographies are computed for each spherical harmonic degree l and order m using the flow solver, complemented by an effective pressure term that accounts for self-gravitation. Because of the large viscosity lateral variations, this procedure is required over simpler methods based on geoid kernels assuming radial viscosity distributions (Richards and Hager, 1984; Ricard et al., 1984). The reader is referred to Zhong et al. (2008) for a more detailed description of the method. Geoid spherical harmonic coefficients $c_{l,m}$ and $s_{l,m}$ are

155 computed at each time step. Geoid undulations $N(\lambda, \phi)$ can then be expressed as a function of latitude λ and longitude ϕ as:

$$N(\lambda, \phi) = R \sum_l \sum_m [\, c_{l,m} \cos\, m\phi + s_{l,m} \sin\, m\phi \,] \, P_l^m(\sin \lambda), \tag{1}$$

where R is Earth's radius, and P_l^m the associated Legendre polynomial of degree l and order m.

For model MF, we consider two different geoid computations. The first one, called "Total geoid" is computed as described above, retaining complete density and viscosity heterogeneities of model MF. The second one, called "No LVVs geoid", cancels

160 out density and viscosity lateral variations in the upper 350 km. More precisely, density lateral variations and flow velocities are first canceled above 350 km depth. Viscosity lateral variations are also removed above 350 km before computing the geoid using the flow solver modified for self-gravitation. In rare cases, the flow solver does not converge. Such a case is found at time -190 Myr in model MF for the "No LVVs geoid" case. We then simply interpolate the geoid computed at times -185 and -195 Myr. The "Total geoid" is rather different from the "No LVVs geoid" because cold slabs in the upper mantle strongly increase

165 the local viscosity, which has a large effect on the surface dynamic topography it produces, hence on the geoid (Flament, 2019). We explore the implications of both choices since several authors only consider radial viscosity variations (e.g., Steinberger, 2016).

Only the total geoid is computed for model MC. However, we first remove density heterogeneities due to the continental material below 250 km depth. This correction removes the spurious effect on the geoid of continental fragments accumulating

170 in the lower mantle.

2.3   True polar wander implementation

TPW is governed by the conservation of Earth's angular momentum, yielding Liouville's equation (Ricard et al., 1993). Here we use a simplified approach to compute TPW by considering that Earth's spin axis aligns instantaneously with the principal axis of greatest inertia (Steinberger and O'Connell, 1997; Zhong et al., 2007). This method neglects the viscous delay due to

175 the Earth's equatorial bulge adjustment.

Those principal axes are obtained from the geoid computed in the mantle convection simulations. The inertia tensor $\mathbf{I}$ due to mass redistribution in the mantle is built from the degree 2 coefficients of the geoid, following MacCullagh's formula (MacCullagh, 1845; Schaber et al., 2009):

$$\mathbf{I} = MR^2 \sqrt{\frac{5}{3}} \begin{pmatrix} \dfrac{c_{2,0}}{\sqrt{3}} - c_{2,2} & -s_{2,2} & -c_{2,1} \\[2mm] -s_{2,2} & \dfrac{c_{2,0}}{\sqrt{3}} + c_{2,2} & -s_{2,1} \\[2mm] -c_{2,1} & -s_{2,1} & -2\dfrac{c_{2,0}}{\sqrt{3}} \end{pmatrix}, \tag{2}$$

180 where M and R are Earth's mass and radius, respectively. The principal inertia axes are then obtained through a diagonalization of this matrix. The axis of greatest inertia corresponds to the largest eigenvalue, while the two equatorial principal axes correspond to the smallest and intermediate eigenvalues. Computing the axis of greatest inertia gives two new poles, one on each side of the planet. Which of the two poles is the "north pole" is arbitrary, and is chosen at the beginning of the simulation.

Name	Surface conditions	Model duration	Δt_{snap}	N_{snap}	$\delta\rho_p$	$\delta\rho_c$	TPW correction
MF0	Plate reconstruction	1000 Myr	5 Myr	201	+73.8 kg m^{-3}	–	None
MF1	Plate reconstruction	1000 Myr	5 Myr	201	+73.8 kg m^{-3}	–	Total geoid
MF2	Plate reconstruction	1000 Myr	5 Myr	201	+73.8 kg m^{-3}	–	No LVVs geoid
MC0	Free-slip	831 Myr[1]	1 Myr	832	+137 kg m^{-3}	-225 kg m^{-3}	None
MC1	Free-slip	831 Myr[1]	1 Myr	832	+137 kg m^{-3}	-225 kg m^{-3}	Total geoid[2]

Table 1. Characteristics of the five mantle convection cases analyzed in this study. Δt_{snap} is the time step between two successive snapshots, and N_{snap} the total number of snapshots. $\delta\rho_p$ an $\delta\rho_c$ are the excess density of chemical piles and deficit density of continents, respectively. [1] Durations of cases MC0 and MC1 correspond to the total duration of model MC minus the 300 first Myr (relaxation time). [2] The geoid is computed after removing the continental material density component below 250 km depth.

TPW is then implemented iteratively by rotating the mantle at each time step to ensure that the spin axis follows the position
185 of the maximum inertia axis. The rotation direction is chosen so that the new north pole remains in the same hemisphere as the previous one, effectively limiting TPW amplitudes to a maximum of 90° per iteration. Since TPW is governed by the geoid, we have two different TPW paths for model MF. In the following, the TPW associated with the total geoid is called "Total TPW", while TPW associated with the no LVVs geoid is called "No LVVs TPW".

This TPW implementation corresponds to a change in the reference frame in which the data are represented. This new
190 reference frame is permanently wandering with respect to the initial simulation frame, we thus call it the wandering frame in the following. The initial simulation is not related to any forcing in the MC model other than the initial conditions. The only preferential relation between the simulation frame and the wandering frame is thus through the initial conditions in the MC model. In contrast, the simulation frame corresponds to the plate tectonics reconstruction frame in model MF. If both plate reconstruction and the resulting mantle convection simulation were perfectly tuned to the Earth, the wandering frame should
195 merge with the simulation frame (to within a rotation in longitude) at the end of the simulation, *i.e.,* for the present time. In past times, the two frames are expected to diverge because of the effect of TPW. In practice, a non-negligible shift exists between the simulation and the wandering frames at the end of the simulation in both the "Total TPW" and "No LVVs TPW" cases.

Spherical harmonic transforms and rotations are performed using the library SHTns (Schaeffer, 2013). SHTns provides an efficient implementation of spherical harmonic rotations based on the stable recursive evaluation of Wigner's d-matrix proposed
200 by Gumerov and Duraiswami (2015), which is accurate up to very large degrees ($> 10^4$).

Five cases are considered in the subsequent analysis of CMB heat flux patterns. Their characteristics are summarized in table 1. Cases MF0 and MC0 are derived from models MF and MC, ignoring TPW. Cases MF1 and MC1 are obtained correcting for the "Total TPW" computed from the "Total geoid" in both models. Case MF2 is derived from the MF model corrected from the "No LVVs TPW", computed from the "No LVVs geoid".

2.4 Principal component analysis of CMB heat flux

We use a principal component analysis (PCA) to obtain the dominant heat flux patterns at the bottom of the mantle in the different models. PCA is a data analysis tool that can be applied to a dataset comprising several observations, each observation depending on several variables. It is used to express the dataset in a new orthonormal basis in order to limit the number of variables needed to explain the data. This is done by computing new variables (called principal components), which are combinations of the initial variables. A full mathematical description of PCA theory is given by Abdi and Williams (2010); see also Pais et al. (2015) for an application to core flows and details of the method. Considering a data set containing I observations described by J variables, the PCA consists in a singular value decomposition of the $I \times J$ data matrix $\mathbf{D}$ as

$$\mathbf{D} = \mathbf{WSP}, \tag{3}$$

where $\mathbf{W}$, $\mathbf{S}$ and $\mathbf{P}$ have respective dimensions $I \times K$, $K \times K$ and $K \times J$, with $K = \min(I, J)$ the rank of the data matrix. $\mathbf{P}$ is a basis of K new variables (or principal components), called p_k with $k \in [\![1 \ ; \ K]\!]$, which are linear combinations of the initial J variables. The amount of data variance explained by p_k decreases with increasing k. It is quantified by a score, called s_k, corresponding to the singular values in the diagonal matrix $\mathbf{S}$. The square of s_k gives the variance explained by p_k. The projections of the I observations on this new basis are stored in the $\mathbf{W}$ matrix.

In the framework of this study, PCA is used to obtain the principal components corresponding to heat flux patterns that explain most of the heat flux signal at the CMB as a function of time. The data set consists in the spherical harmonics coefficients of q_{CMB} for each snapshot of the mantle convection model, truncated at a maximum degree $l_{max} = 50$. PCA requires data to be centered, which means in our case that the mean of each spherical harmonic coefficient on the whole time series has to be removed. This operation is equivalent to removing the mean heat flux pattern $\overline{q}(\lambda, \phi)$ from the time series. Following previously described notations, the kth PCA component consists in a J-dimension vector $p_k(l, m)$ of spherical harmonic coefficients, a score called s_k, and a time-dependent weight $w_k(t)$. We note $\tilde{p}_k(\lambda, \phi)$ the heat flux pattern reconstructed from the $p_k(l, m)$ spherical harmonic coefficients. For each component, a time-dependent amplitude A_k can be defined as $A_k(t) = w_k(t) \times s_k$. Because of data centering, the heat flux patterns of the PCA components have to be interpreted as perturbations to the mean heat flux pattern.

Once PCA is performed, time-dependent CMB heat flux maps can be reconstructed as:

$$q_{CMB}(\lambda, \phi, t) = \overline{q}(\lambda, \phi) + \sum_{k=1}^{K} w_k(t) \, s_k \, \tilde{p}_k(\lambda, \phi). \tag{4}$$

The first components give the highest contribution to the full variability of CMB heat flux. They provide plausible CMB heat fluxes that can also be applied as boundary conditions in dynamo calculations.

3 Results

Let us first present and discuss important characteristics of the two mantle simulations we exploit. Selected snapshots of topography, basal heat flux, and geoid undulations, are shown in Fig. 1 and Fig. 2 for models MF and MC, respectively.

Both models reproduce the well-known bimodal topography of the Earth, reflecting the difference between continental and oceanic crusts. Oceanic ridges and trenches are well marked. Present tectonic plates are easily recognized in line "0 Myr" of model MF in Fig. 1, and topography snapshots at -300, -600 and -900 Myr are identical to corresponding "No Net Rotation" plate configurations of Merdith et al. (2021) shown in Fig. 2 of Müller et al. (2022). Let us recall that mantle simulation MF is

240   driven by plates, while plates spontaneously form and move in mantle simulation MC and note that MC plates look similar to those of model MF (Fig. 2).

CMB heat flux maps of both models show large-scale variations that strongly correlate with the presence of basal chemical piles (delineated by black lines). The heat flux is low beneath these piles, which act as thermal insulators. In both models, chemical piles are shaped and pushed by cold slabs that reach the CMB. Note that the mean basal heat flux is about four times

245   larger in MF than in MC.

3.1   Geoid

Our study requires computing the geoid in our models, in order to deduce the resulting TPW. The geoid stems from a delicate balance between bulk density heterogeneities and flow-induced interface undulations. The two simulations have very different geoids. The total geoid of models MF and MC differ in amplitude almost by a factor of 10 (first columns of Fig. 1 and Fig.

250   2). While the geoid amplitude in MF are twice those of the present Earth, geoid amplitudes in MC are much larger. Geoid highs in MC appear to be correlated with continents and subduction zones, while oceanic ridges yield geoid lows. In contrast, continents do not appear in geoid undulations in MF while subducted oceanic slabs are associated with well-defined geoid lows. The presence of cold and very viscous slabs in the upper mantle has a strong effect on the geoid. We evaluate this effect by computing the "No LVVs geoid", shown in the second column of Fig. 1. We recall that this alternative geoid is computed

255   after removing density and viscosity heterogeneities in the upper 350 km of the mantle. The sharp signature of oceanic trenches indeed disappears, but geoid undulations are almost twice as large, and differ substantially from those of the "Total geoid". The two geoids are nonetheless rather similar at the beginning of the simulation (see snapshot at -900 Myr) and to a lesser extent at the end of the simulation (see snapshot at 0 Myr). Another important difference between the "Total geoid" and the "No LVVs geoid" is their time variability: the successive updates of subducting slabs in model MF tend to produce small and

260   rapid changes in the geoid that impact TPW predictions. Note that neither MF nor MC model shows a clear correlation between geoid highs and the position of basal chemical piles.

3.2   TPW correction

TPW is applied by computing the successive positions of the maximum inertia axis and rotating the simulation frame to align this axis with the spin axis. The successive positions of the maximum inertia axis in the simulation frames of models MF

265   and MC for cases MF1, MF2 and MC1 are shown in Fig. 3. These successive positions represent the TPW path in each case. No TPW correction would be required if the maximum inertia axis stayed fixed at either pole of these frames. The rotation compared to the simulations frames due to the TPW correction is the largest when the maximum inertia axis plots at the equator.
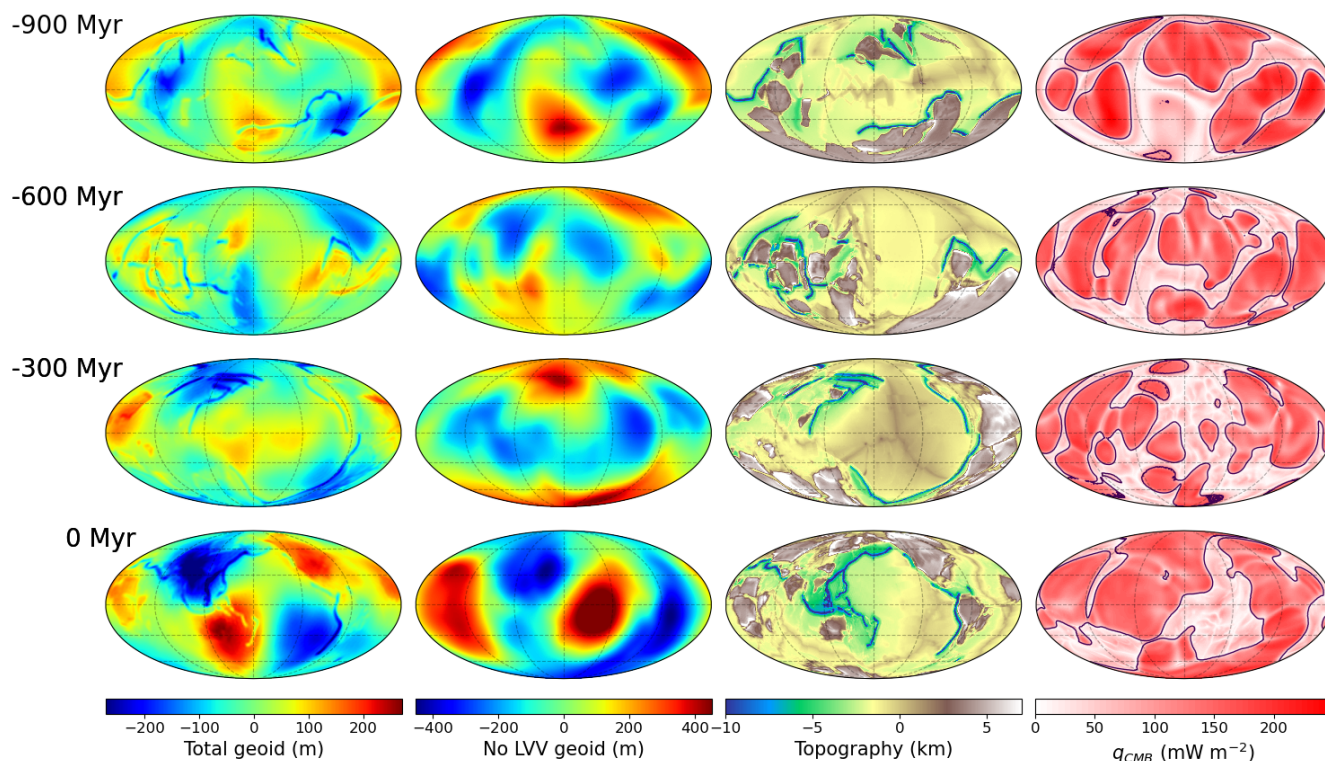
Figure 1. Model MF. Maps of geoid undulations (first column: "Total geoid"; second column: "No LVVs geoid"), surface topography (third column), and CMB heat flux (last column) at selected times. The maps are shown in a Mollweide projection. Black lines in the heat flux maps delineate the edges of basal chemical piles. The heat flux is low beneath chemical piles.

Let us analyze the TPW paths for model MF, computed either from the "Total geoid" (MF1) or the "No LVVs geoid" (MF2). The present-day position (black-circled magenta disk in Fig. 3) of the maximum inertia axis is similar in both cases. Since MF
270   model satisfies plate configuration at $t = 0$, this axis should plot at one pole of the simulation if it faithfully reproduced actual mantle configuration. This is not precisely the case, but we observe that the TPW path for MF1 remains at high latitudes for the past 300 Myr, a period of time when paleoplate reconstruction includes constraints from magnetic pole position. Further back in time, there is no reason for the 'no net rotation' frame used in model MF to match the spin frame. We observe that MF1 and MF2 TPW paths rapidly diverge. However, during the first 150 Myr of the simulation, the poles in MF1 versus MF2
275   are almost antipodal, meaning that the inertia axis are almost aligned. This is consistent with the similar geoid patterns in both cases at -900 Myr shown on Fig. 1. Note that the TPW path for MF1 is very irregular. This scatter of the maximum inertia axis position is due to a large time variability in the "Total geoid", induced notably by the updates of subduction zones every 1 Myr. Interestingly, an inertia interchange TPW (IITPW) event occurs in MF1 between -425 Myr and -420 Myr. This event is highlighted by a black arrow on Fig. 3. An IITPW event happens when the maximum inertia axis and the intermediate inertia
280   axis switch order, resulting in a $\sim 90°$ rotation between the two successive time steps. Such kind of events have been suggested
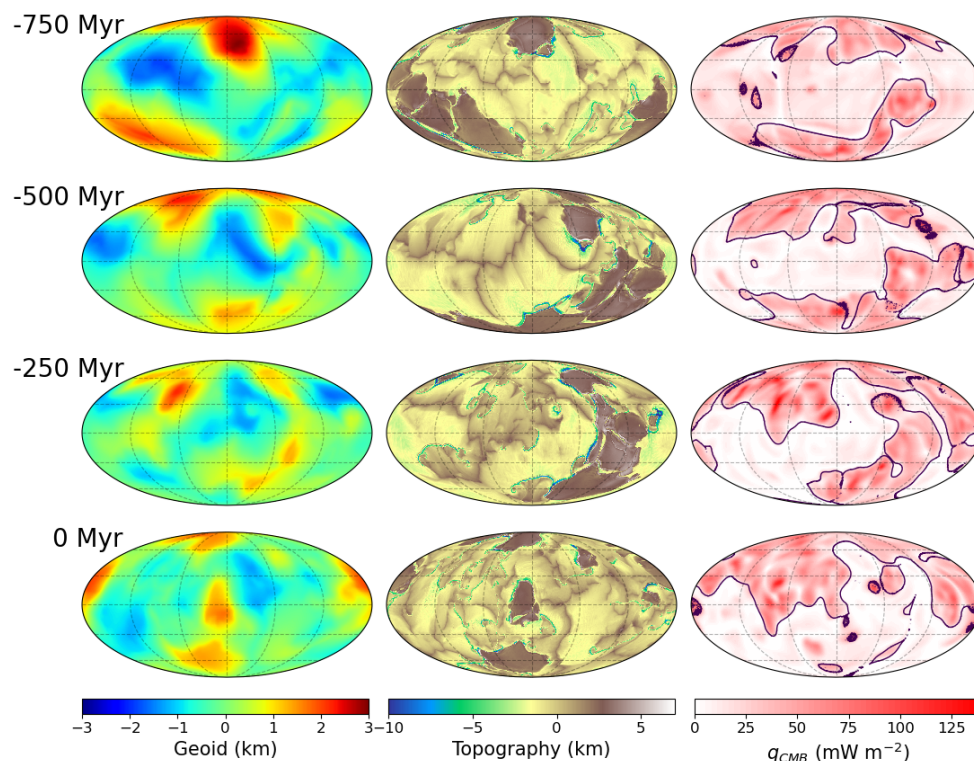
Figure 2. Model MC. Maps of geoid undulations (left), surface topography (center), and CMB heat flux (right) at selected times. The maps are shown in a Mollweide projection. Black lines in the heat flux maps delineate the edges of basal chemical piles. Heat flux is low beneath chemical piles.
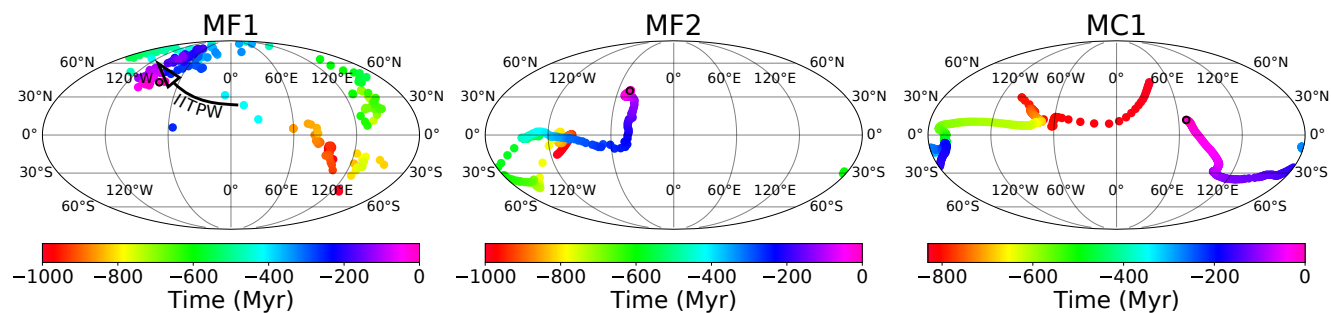

Figure 3. TPW paths in cases MF1, MF2 and MC1 in a Mollweide projection. Color disks represent the successive positions of the maximum inertia axis in the simulation frames. The color scale gives the time before the end of the simulation in Myr. Black-circled magenta disk shows the position of the maximum inertia axis at the end of the simulation. The Inertia Interchange TPW event (IITPW) in case MF1 is highlighted by the black arrow.
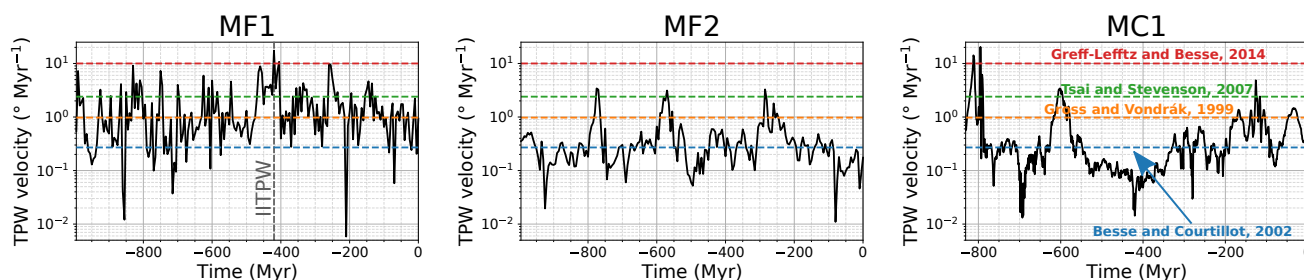
Figure 4. TPW velocity in $^\circ$ Myr^{-1} as a function of time in cases MF1, MF2, and MC1. The horizontal dashed lines give some values from the literature. Besse and Courtillot (2002): Velocities during past TPW events in the last 200 Myr; Gross and Vondrák (1999): Present-day TPW velocities; Tsai and Stevenson (2007): Maximum TPW velocity value for the present-day mantle; Greff-Lefftz and Besse (2014): Maximum modeled TPW velocity for an inertia interchange event.

as an explanation of fast apparent polar wander in the Cambrian and Ediacarian periods (Kirschvink et al., 1997; Robert et al., 2017).

Turning to model MC, we recall that this model is not related to any plate reconstruction. Hence no particular relationship is expected between the simulation frame and the wandering frame. However, the two frames are linked due to the relationship

285 between chemical piles and the geoid in the model. Chemical piles are introduced at the equator at the beginning of the simulation, and remain at low latitudes by spreading around the equator. These piles are mostly associated with geoid lows throughout the simulation. They thus tend to move from low latitudes towards high latitudes due to the TPW correction. As a result, the maximum inertia axis tends to form a $\sim 90^\circ$ angle with the z-axis of the simulation frame, and only drift in longitude, as observed in Fig. 3.

290 The time evolution of TPW velocities (in $^\circ$ Myr^{-1}) for the different models is shown in Fig. 4. Those velocities are compared to values from the literature represented as horizontal dashed lines: Besse and Courtillot (2002) give a typical velocity of 0.27° Myr^{-1} during TPW events in the last 200 Myr; Gross and Vondrák (1999) measure a present-day TPW velocity of 0.98° Myr^{-1}; Tsai and Stevenson (2007) find 2.4° Myr^{-1} as a maximum TPW velocity reachable for the present-day mantle; Greff-Lefftz and Besse (2014) obtain TPW velocities up to 10° Myr^{-1} during an IITPW event in simplified mantle convection

295 models. In all our cases, TPW velocities are roughly contained between 0.01° Myr^{-1} and 10° Myr^{-1}. Note that because of the 5 Myr time step between two successive snapshots in model MF, TPW velocity cannot be higher than 18° Myr^{-1} for MF1 and MF2. Similarly in MC1, TPW velocity is limited to 90° Myr^{-1} by the 1 Myr time step. The average TPW velocity is $\sim 1.79^\circ$ Myr^{-1} in MF1. This is much faster than in MF2 and MC1, with averaged TPW velocities $\sim 0.55^\circ$ Myr^{-1} and $\sim 0.63^\circ$ Myr^{-1}, respectively. This faster TPW rate is related to the greater scatter of successive inertia axis positions in MF1 compared to MF2

300 and MC1. These larger TPW velocities are thus directly related to the updating of surface conditions that implies a large time variability of the "Total geoid" in the MF simulation. In contrast, TPW velocities of MF2 and MC1 are very similar, despite an order of magnitude difference in the amplitude of their geoid (see Fig. 1 and Fig. 2). The highest velocity peak at -420 Myr in MF1 reaches 17.5° Myr^{-1}. This corresponds to a rotation of 87° in one time step. Such a large rotation is due to the IITPW
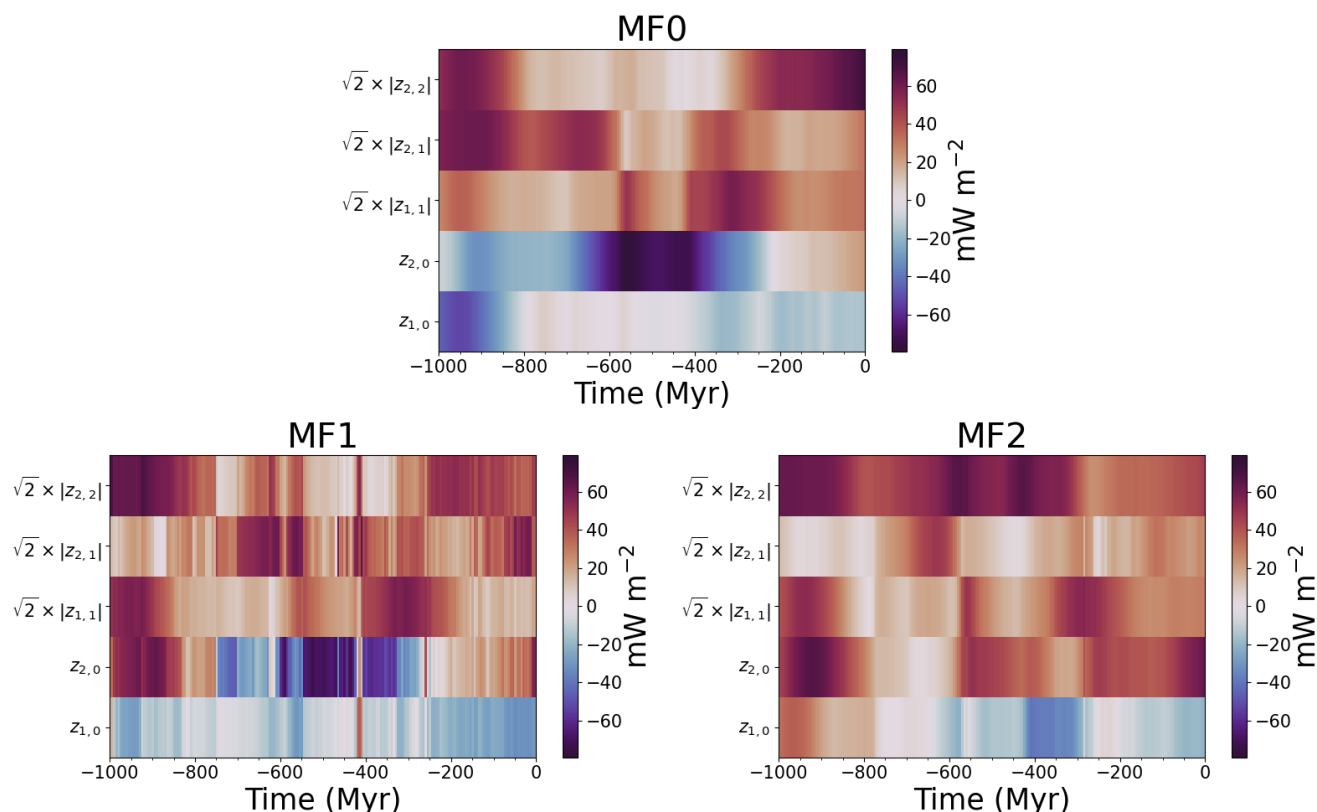
Figure 5. Time evolution of degree 1 and 2 spherical harmonic coefficients of the CMB heat flux in cases MF0, MF1 and MF2.

event occurring between -425 Myr and -420 Myr. This velocity is greater than the one obtained by Greff-Lefftz and Besse

305 (2014) for an IITPW event in simplified mantle models, although Robert et al. (2017) obtained similar values for the maximum velocity reached for a specific IITPW event during Ediacarian times. One should however keep in mind that we neglected the time delay due to the equatorial bulge adjustment in our TPW correction.

3.3 CMB heat flux

3.3.1 Time variability of large-scale patterns

310 Most studies exploring the effect of CMB heat flux heterogeneity on the geodynamo focused on large-scale patterns of spherical harmonic degree 1 and 2 (Glatzmaier et al., 1999; Olson and Christensen, 2002; Kutzner and Christensen, 2004; Olson et al., 2010). We thus first examine the time evolution of these patterns in the different cases. The amplitude of degree 1 and 2 spherical harmonic coefficients of CMB heat flux are shown in Fig. 5 for cases MF0, MF1 and MF2, and in Fig. 6 for cases MC0 and MC1. As expected, low-degree patterns evolve rather smoothly, on mantle convection timescales of several hundreds

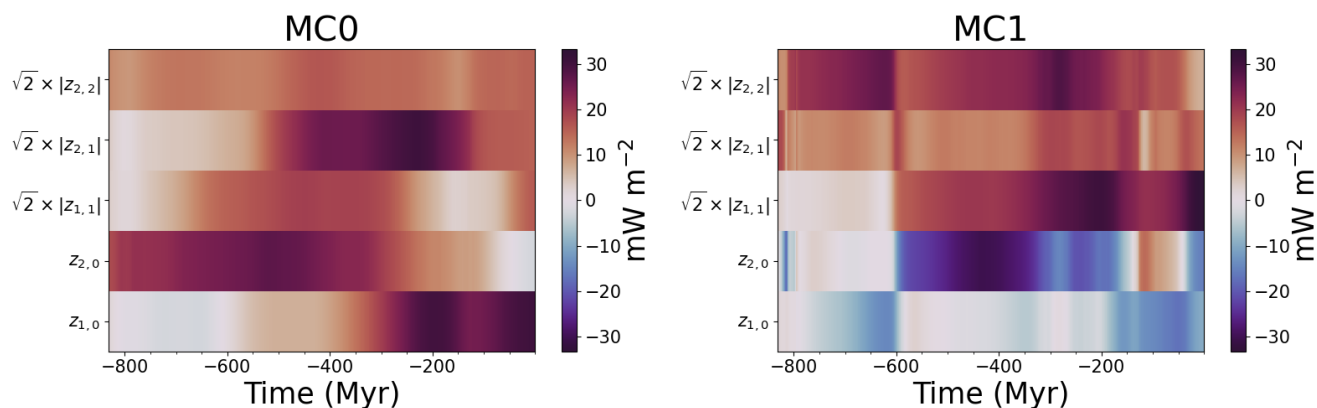315 of million years, in cases MF0 and MC0.

13

Figure 6. Time evolution of degree 1 and 2 spherical harmonic coefficients of CMB heat flux in cases MC0 and MC1.

We have seen that CMB heat flux variations are strongly controlled by the distribution of basal chemical piles in our models. When piles are at high latitudes for example at -600 Myr in model MF0 (see Fig. 1), the CMB heat flux is greater around the equator, yielding a negative $z_{2,0}$ coefficient. Inversely, with mostly equatorial piles at time -500 Myr, model MC0 has a strong positive $z_{2,0}$ coefficient at that time. The end of MF0 is dominated by the degree 2 and order 2 component. This pattern
320   is expected at the end of the MF0 case, as model MF reproduces the present-day positions of the observed antipodal LLVPs below Africa and the Pacific (see Fig. 1).

True polar wander strongly impacts the behavior of large-scale CMB heat flux patterns. We first note that TPW can modify the hierarchy of these patterns. For example, while the $z_{1,0}$ coefficient largely dominates in the last 100 Myr of MC0, $z_{1,1}$ takes over in the TPW corrected MC1 case. TPW can also change the sign of these coefficients. The piles spreading at the equator
325   in model MC translates into a large positive $z_{2,0}$ coefficient (weaker heat flux around the equator) in MC0. This coefficient becomes negative in MC1 because the piles are moved towards higher latitudes by the TPW. Similarly, $z_{2,0}$ is negative during most of the time in MF0, but remains positive due to TPW in MF2. This is not the case in MF1, suggesting that the piles are more correlated with the "No LVVs geoid" than with the "Total geoid".

More importantly, our study reveals that true polar wander can change large-scale patterns of CMB heat flux on timescales
330   much shorter than typical mantle convection timescales. This is well illustrated by several sign reversals of the $z_{2,0}$ coefficient in case MF1, which occur over time lapses shorter than 10 Myr. This is notably the case during the IITPW event between -425 Myr and -420 Myr. Of course, the large amount of fast changes in the spherical harmonic coefficients for MF1 is due to the rather rapid variations of the "Total geoid" computed from model MF. Nevertheless, slightly less rapid events are also visible in MF2 and MC1.
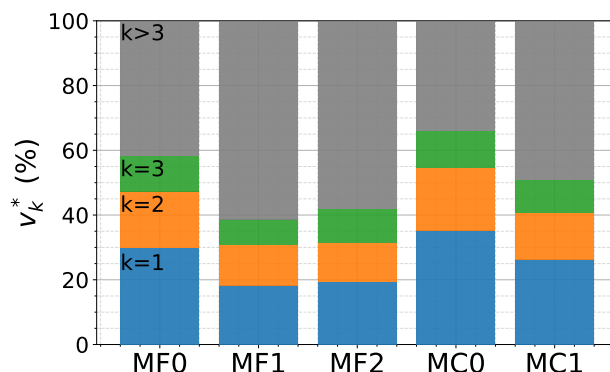
Figure 7. Variance explained by the first three PCA components normalized by the total variance in the different cases.

3.3.2 Principal component analysis of the CMB heat flux

As mentioned earlier, exploration of the effect of CMB heat flux heterogeneities on the geodynamo has previously mostly been focused on degrees 1 and 2. An alternative is to explore the effect of heterogeneities inferred from seismic tomography of the lowermost mantle (Olson et al., 2010; Mound and Davies, 2023). However, the latter approach is only appropriate to describe the present core-mantle coupling, assuming the conversion of seismic tomography to temperature is well understood. In order to assess past geodynamo behavior, one would like to test the effect of plausible past CMB heat flux patterns and amplitudes. Snapshots of the heat flux maps we computed could be used for this purpose. Another possibility is to examine what are the dominant heat flux patterns, and how they evolve in time. This is what we propose, using a principal component analysis (PCA).

PCA results consist in a set of components, ranked by decreasing contribution to the total CMB heat flux variations. Each component is described by a heat flux pattern and an amplitude. The amount of variance v_k explained by the kth PCA component is given by the square of the associated score: $v_k = s_k^2$.

The variance explained by the first three PCA components is shown in Fig. 7. These components account for 57% and 65% of the total variance in cases MF0 and MC0, respectively. The amount of variance explained by the first three component is lower in TPW-corrected cases, with values reaching 38%, 41% and 50% for cases MF1, MF2, and MC1, respectively. These lower values are due to the addition of a source of time variability in the CMB heat flux when TPW is considered. Among the TPW-corrected cases, the explained variance is the lowest in MF1. This can be related to TPW velocities, which are the fastest on average in case MF1, increasing the time variability.

The patterns of the first three PCA components are shown in Fig. 8 for cases MF0, MF1 and MF2, and in Fig. 9 for cases MC0 and MC1. Those patterns are perturbations to the average heat flux pattern, also shown in the figures for each case.

The associated amplitudes of the first three PCA components are shown in Fig. 10 for cases MF0, MF1 and MF2, and in Fig. 11 for cases MC0 and MC1. The amplitudes of the first PCA components mostly vary on large time scales. However, the TPW
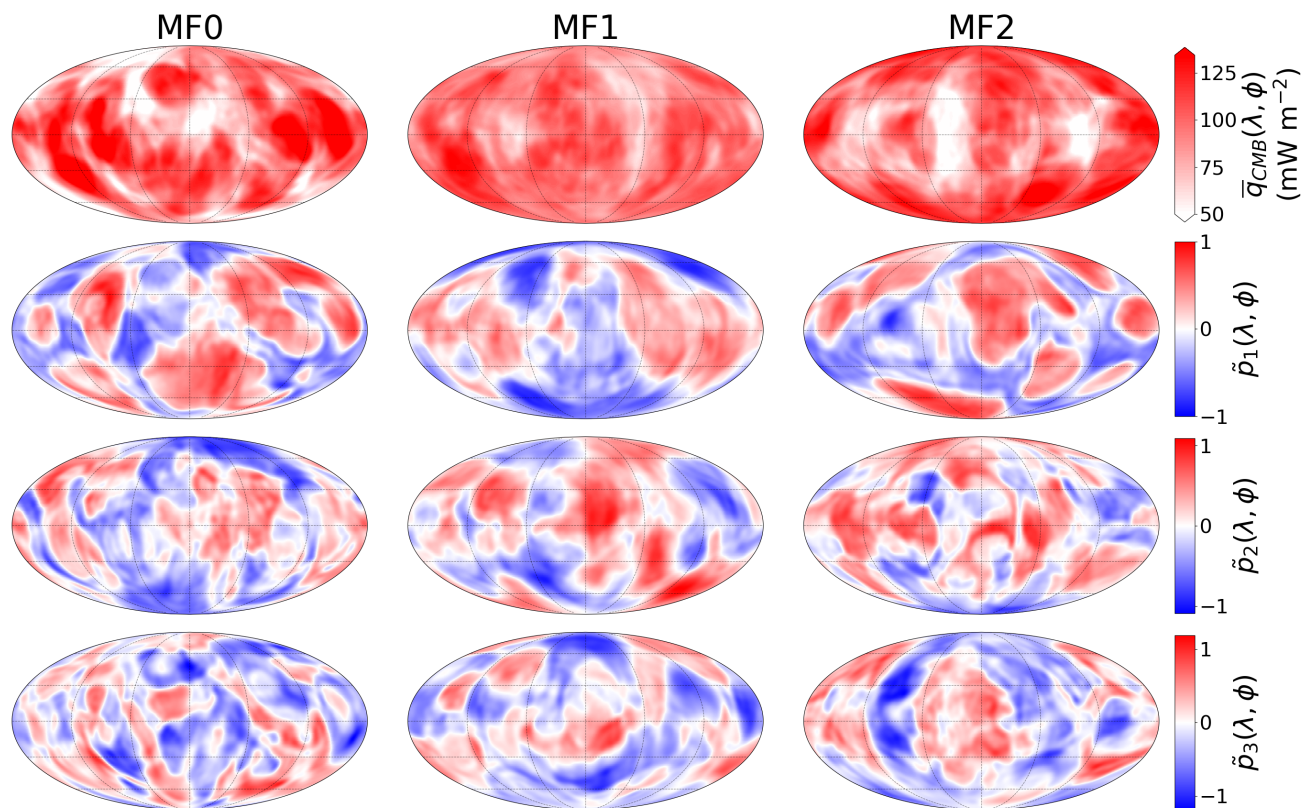
15

Figure 8. Patterns of the first three PCA components of the CMB heat flux $\tilde{p}_1$, $\tilde{p}_2$ and $\tilde{p}_3$ in cases MF0, MF1 and MF2. The averaged heat flux pattern is given in the top line for each case. The maps are shown in a Mollweide projection.

corrected models display amplitude variations at much higher frequencies, due to the time variability added by TPW. This is particularly visible for case MF1, which displays the largest TPW velocities.

4 Discussion

360 Recent models offer the possibility to study mantle convection related to plate tectonics on timescales of the order of 1 Gyr. These models reproduce plate tectonics either self-consistently (Coltice et al., 2019) or using plate reconstruction that have been extended to cover the last 1 Gyr by recent works (Merdith et al., 2021). Both kinds of models enable to study the relation between surface tectonics and the structure of the lower mantle (Flament et al., 2022; Cao et al., 2021). The CMB heat flux is of particular interest for the geodynamo (Glatzmaier et al., 1999; Kutzner and Christensen, 2004; Olson et al., 2010). However,

365 TPW needs to be incorporated to these models in order to study the relation between CMB heat flux and the geodynamo. In this study, we performed the exploitation of two such large recent mantle convection simulations by correcting these models for the TPW in order to obtain the CMB heat flux in the frame appropriate for the geodynamo.
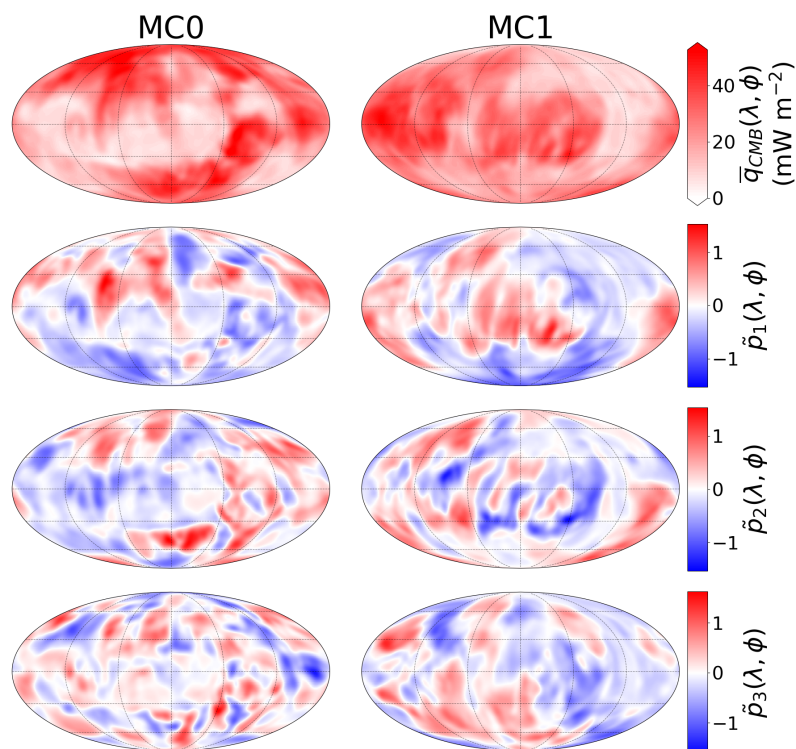
Figure 9. Patterns of the first three PCA components of the CMB heat flux $\tilde{p}_1$, $\tilde{p}_2$ and $\tilde{p}_3$ in cases MC0 and MC1. The averaged heat flux pattern is given in the top line for each case. The maps are shown in a Mollweide projection.

4.1 Impact of TPW on CMB heat flux

In the two mantle convection models studied here, we find that correcting for the TPW induces fast variations of the CMB heat flux, even at low spherical harmonic degrees. These fast variations, illustrated in Fig. 5 and Fig. 6, can induce changes in the hierarchy of spherical harmonic modes, and in the sign of the coefficients. The TPW induced variations do not originate from a change in the flux pattern but rather from a global rotation of a given pattern. Though mantle convection is completely unaffected by global rotations of the mantle, it can be of great importance for the core. The latitudinal distribution of the CMB heat flux has indeed been shown to play a role in geodynamo simulations (Glatzmaier et al., 1999; Kutzner and Christensen, 2004; Olson et al., 2010). TPW has thus been suggested by several authors as a source of time variation for the geodynamo, notably concerning the reversal frequency of the magnetic dipole (Courtillot and Besse, 1987; Zhang and Zhong, 2011; Biggin et al., 2012). These fast TPW-induced time variations could thus be related to abrupt changes of the magnetic dipole behavior such as the emergence or the end of superchrons. It is all the more important to consider these variations that they can occur on timescales potentially faster than typical variations originating solely from mantle convection. As well as short timescales, the CMB heat flux outputs in the different cases includes small length scales. Those small scales can be seen in the heat flux

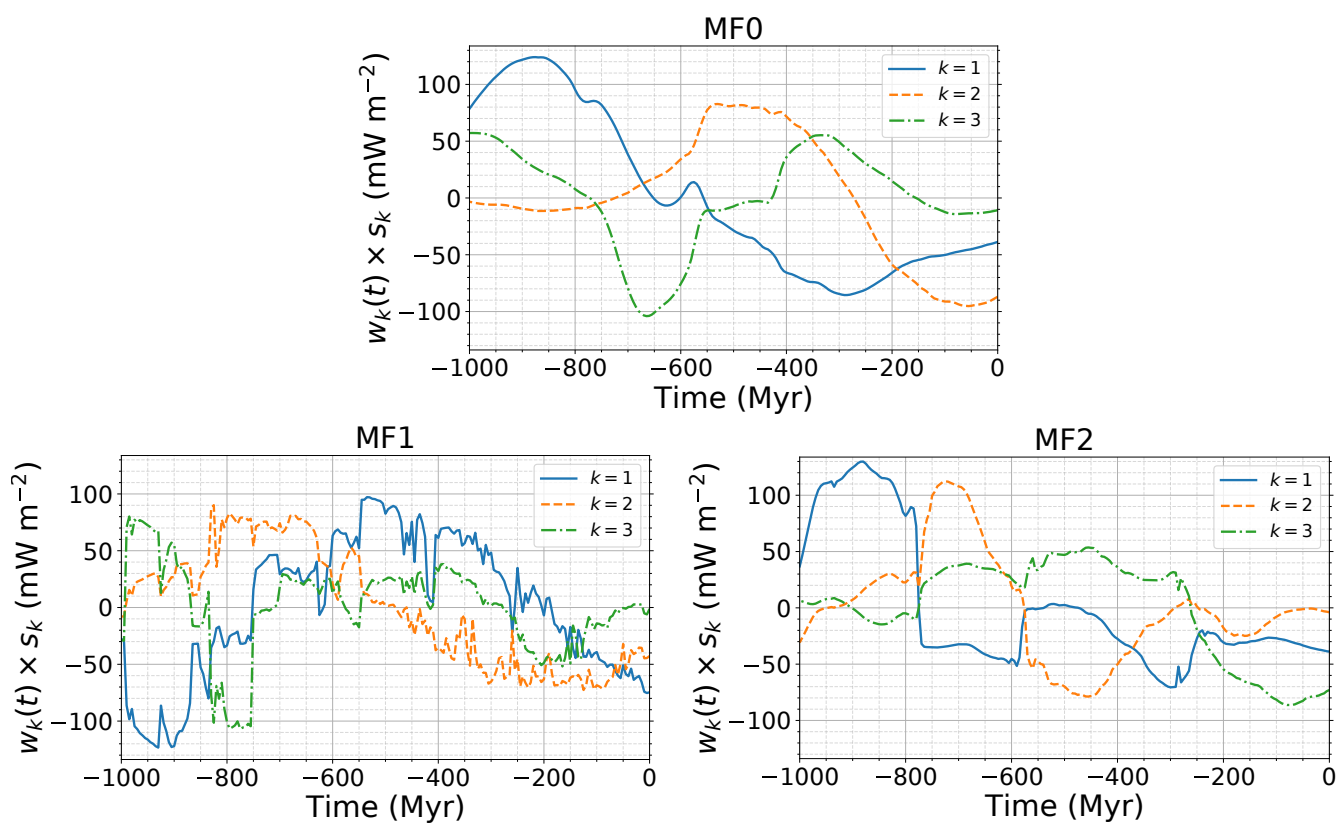**Figure 10.** Time-evolution of the amplitudes of the first three PCA components of the CMB heat flux for cases MF0, MF1 and MF2.
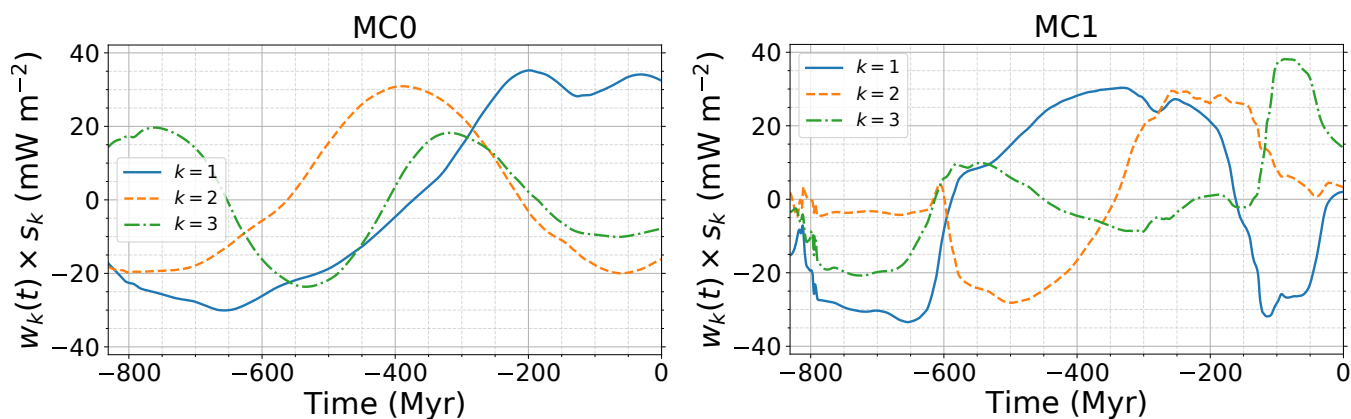

Figure 11. Time-evolution of the amplitudes of the first three PCA components of the CMB heat flux for cases MC0 and MC1.

snapshots of Fig. 1 and Fig. 2, and they also appear in the patterns of the first PCA components in Fig. 8 and Fig. 9. Attempts to relate geodynamo models with mantle convection have previously been made using either degree 1 or 2 fixed heat flux patterns, or tomographic patterns derived from seismic tomography (Olson et al., 2010; Terra-Nova et al., 2019; Mound and Davies, 2023). These attempts either overlook the effect of small scales in the CMB heat flux, or focus on a present-day heat
385 flux pattern which may not be representative of the history of Earth's mantle convection.

4.2 PCA of the CMB heat flux

The different PCA we computed give the dominant heat flux patterns for each case. The PCA components of the CMB heat flux largely reflects the positions of the piles. The insulating effect of the piles indeed dominates the large scales of the CMB heat flux. The dominant length scales of the heat flux patterns tend to decrease with the PCA component number, but the length
390 scale separation between the three first components is rather weak. It is particularly true for the TPW corrected cases. This is due to the addition of a source of complexity in these cases, which results in more different large scales patterns required to explain the CMB heat flux time series. This additional source of complexity in the dataset also translates in a smaller amount of variance explained by the first PCA components, as shown in Fig. 7.

4.3 Limitations and perspectives

395 The geoids corresponding to cases MF1, MF2 and MC1 widely differ in terms of amplitudes and patterns. In the MF model, subduction zones are associated with thin negative anomalies in the "Total geoid" case (MF1) which does not appear in the "No LVVs geoid" case (MF2). As for the MC model, the geoid shows positive anomalies over subduction zones, as well as over continents which are not correlated with the two different geoids in model MF. The geoid anomalies amplitude are larger than the observed anomalies on Earth in the three cases but by widely different magnitude, from about twice the observed anomalies
400 for the "Total geoid" of model MF to more than 10 times the observed anomalies in model MC. This illustrates shortcomings that still exist in mantle convection models concerning the geoid computation. The mismatch between model geoids and the observed geoid is an important limitation of this study. Improvement in the mantle convection models are required to obtain a geoid behaving closer to the expectations, and with more consistency between the different models. Despite this limitation, we still obtain TPW velocities consistent with the literature. This is expected since our simplified approach in which TPW is
405 entirely controlled by the shape of the geoid, independently of its amplitude. The improvement of the geoid computation should thus not affect our conclusion on the addition of small timescale variations in the CMB heat flux due to TPW. Interestingly, the positions of the pole in case MF1 is close to the pole of the plate reconstruction for a large part of model MF, notably between -150 Myr and -600 Myr. During this period of time, the average angle between the z-axis of the plate reconstruction frame and the maximum inertia axis is of $\sim 26.3°$. The TPW correction compared to the plate reconstruction frame is thus rather
410 small for this period of time. This is however not the case for the rest of the time in MF1 and for the full MF2 case. To be fully self-consistent, mantle convection models based on plate reconstruction should add constraints from the TPW to avoid this discrepancy between the inertia axis and the z-axis of the plate reconstruction.

5 Conclusion

The two main goals of this work are to investigate how TPW can affect the CMB heat flux in term of space and time behavior,
415 and to provide heat flux maps representative of ∼1 Gyr of mantle evolution in a reference frame useful for geodynamo models.
Notwithstanding current limitations in predicting the geoid from forward mantle convection models, we show that TPW can
greatly affect the large scales of the CMB heat flux by changing the hierarchy between low-degree spherical harmonics modes,
changing the sign of these modes, and by adding time variations on short time scales of the order of a few million years.
We performed a PCA to obtain the dominant heat flux patterns at the CMB in the different cases. These patterns represent a
420 temporal average and they preserve small length scales that could be important for the dynamo action. These patterns can thus
be used as alternative to snapshots to couple the mantle convection models with geodynamo models. An important finding of
this study is the lack of convergence in the geoid associated with the mantle convection models. The obtained geoid are vastly
different between the two models, and depending on wether lateral variations in the upper mantle are included. Although the
effects of the TPW on the CMB heat flux that we observe here are expected even with a more realistic geoid, it would be of
425 great interest to understand where these discrepancies come from.

435 **References**

Abdi, H. and Williams, L. J.: Principal component analysis, WIREs Comp Stat, 2, 433–459, https://doi.org/10.1002/wics.101, 2010.

Amit, H., Choblet, G., Olson, P., Monteux, J., Deschamps, F., Langlais, B., and Tobie, G.: Towards more realistic core-mantle boundary heat flux patterns: a source of diversity in planetary dynamos, Prog. in Earth and Planet. Sci., 2, 26, https://doi.org/10.1186/s40645-015-0056-3, 2015.

440 Arnould, M., Coltice, N., Flament, N., and Mallard, C.: Plate tectonics and mantle controls on plume dynamics, Earth and Planetary Science Letters, 547, 116 439, https://doi.org/10.1016/j.epsl.2020.116439, 2020.

Besse, J. and Courtillot, V.: Apparent and true polar wander and the geometry of the geomagnetic field over the last 200 Myr, J. Geophys. Res., 107, EPM 6–1–EPM 6–31, https://doi.org/10.1029/2000JB000050, 2002.

Biggin, A. J., Steinberger, B., Aubert, J., Suttie, N., Holme, R., Torsvik, T. H., van der Meer, D. G., and van Hinsbergen, D. J. J.: Possible links between long-term geomagnetic variations and whole-mantle convection processes, Nature Geosci, 5, 526–533, https://doi.org/10.1038/ngeo1521, 2012.

Billen, M. I.: Modeling the dynamics of subducting slabs, Annu. Rev. Earth Planet. Sci., 36, 325–356, 2008.

Bower, D. J., Gurnis, M., and Flament, N.: Assimilating lithosphere and slab history in 4-D Earth models, Physics of the Earth and Planetary Interiors, 238, 8–22, 2015.

450 Burke, K., Steinberger, B., Torsvik, T. H., and Smethurst, M. A.: Plume Generation Zones at the margins of Large Low Shear Velocity Provinces on the core–mantle boundary, Earth and Planetary Science Letters, 265, 49–60, https://doi.org/10.1016/j.epsl.2007.09.042, 2008.

Cambiotti, G., Ricard, Y., and Sabadini, R.: New insights into mantle convection true polar wander and rotational bulge readjustment, Earth and Planetary Science Letters, 310, 538–543, 2011.

455 Cao, X., Flament, N., and Müller, R. D.: Coupled evolution of plate tectonics and basal mantle structure, Geochemistry, Geophysics, Geosystems, 22, e2020GC009 244, 2021.

Coltice, N., Husson, L., Faccenna, C., and Arnould, M.: What drives tectonic plates?, Sci. Adv., 5, eaax4295, https://doi.org/10.1126/sciadv.aax4295, 2019.

Courtillot, V. and Besse, J.: Magnetic field reversals, polar wander, and core-mantle coupling, Science, 237, 1140–1147, 1987.

460 Crameri, F., Tackley, P., Meilick, I., Gerya, T., and Kaus, B.: A free plate surface and weak oceanic crust produce single-sided subduction on Earth, Geophysical Research Letters, 39, 2012.

Davaille, A. and Romanowicz, B.: Deflating the LLSVPs: Bundles of Mantle Thermochemical Plumes Rather Than Thick Stagnant "Piles", Tectonics, 39, https://doi.org/10.1029/2020TC006265, 2020.

Durand, S., Debayle, E., Ricard, Y., Zaroli, C., and Lambotte, S.: Confirmation of a change in the global shear velocity pattern at around 465 1000 km depth, Geophysical Journal International, 211, 1628–1639, 2017.

Dziewonski, A. M. and Anderson, D. L.: Preliminary reference Earth model, Physics of the earth and planetary interiors, 25, 297–356, 1981.

Dziewonski, A. M., Hager, B. H., and O'Connell, R. J.: Large-scale heterogeneities in the lower mantle, Journal of Geophysical Research, 82, 239–255, 1977.

Flament, N.: Present-day dynamic topography and lower-mantle structure from palaeogeographically constrained mantle flow models, Geo-470 physical Journal International, 216, 2158–2182, 2019.

Flament, N., Bodur, Ö. F., Williams, S. E., and Merdith, A. S.: Assembly of the basal mantle structure beneath Africa, Nature, 603, 846–851, 2022.

Garnero, E. J. and Helmberger, D. V.: A very slow basal layer underlying large-scale low-velocity anomalies in the lower mantle beneath the Pacific: evidence from core phases, Physics of the Earth and Planetary Interiors, 91, 161–176, 1995.

475 Garnero, E. J. and McNamara, A. K.: Structure and dynamics of Earth's lower mantle, science, 320, 626–628, 2008.

Glatzmaier, G. A., Coe, R. S., Hongre, L., and Roberts, P. H.: The role of the Earth's mantle in controlling the frequency of geomagnetic reversals, Nature, 401, 885–890, https://doi.org/10.1038/44776, 1999.

Goldreich, P. and Toomre, A.: Some remarks on polar wandering, Journal of Geophysical Research, 74, 2555–2567, https://doi.org/10.1029/JB074i010p02555, 1969.

480 Greff-Lefftz, M. and Besse, J.: Sensitivity experiments on True Polar Wander, Geochem. Geophys. Geosyst., 15, 4599–4616, https://doi.org/10.1002/2014GC005504, 2014.

Gross, R. S. and Vondrák, J.: Astrometric and space-geodetic observations of polar wander, Geophys. Res. Lett., 26, 2085–2088, https://doi.org/10.1029/1999GL900422, 1999.

Gumerov, N. A. and Duraiswami, R.: Recursive computation of spherical harmonic rotation coefficients of large degree, in: Excursions in
485 Harmonic Analysis, Volume 3: The February Fourier Talks at the Norbert Wiener Center, pp. 105–141, Springer, 2015.

Kirschvink, J. L., Ripperdan, R. L., and Evans, D. A.: Evidence for a large-scale reorganization of Early Cambrian continental masses by inertial interchange true polar wander, Science, 277, 541–545, 1997.

Kutzner, C. and Christensen, U. R.: Simulated geomagnetic reversals and preferred virtual geomagnetic pole paths, Geophysical Journal International, 157, 1105–1118, https://doi.org/10.1111/j.1365-246X.2004.02309.x, 2004.

490 Lay, T. and Helmberger, D. V.: A shear velocity discontinuity in the lower mantle, Geophysical Research Letters, 10, 63–66, 1983.

Liu, X. and Zhong, S.: The long-wavelength geoid from three-dimensional spherical models of thermal and thermochemical mantle convection, J. Geophys. Res. Solid Earth, 120, 4572–4596, https://doi.org/10.1002/2015JB012016, 2015.

MacCullagh, J.: On the rotation of a solid body, Proceedings of the Royal Irish Academy, 3, 370–371, 1845.

Merdith, A. S., Williams, S. E., Collins, A. S., Tetley, M. G., Mulder, J. A., Blades, M. L., Young, A., Armistead, S. E., Cannon, J., Zahirovic,
495 S., et al.: Extending full-plate tectonic models into deep time: Linking the Neoproterozoic and the Phanerozoic, Earth-Science Reviews, 214, 103 477, 2021.

Mosca, I., Cobden, L., Deuss, A., Ritsema, J., and Trampert, J.: Seismic and mineralogical structures of the lower mantle from probabilistic tomography, J. Geophys. Res., 117, https://doi.org/10.1029/2011JB008851, 2012.

Mound, J. E. and Davies, C. J.: Longitudinal structure of Earth's magnetic field controlled by lower mantle heat flow, Nature Geoscience,
500 16, 380–385, https://doi.org/10.1038/s41561-023-01148-9, 2023.

Müller, R. D., Cannon, J., Tetley, M., Williams, S. E., Cao, X., Flament, N., Bodur, Ö. F., Zahirovic, S., and Merdith, A.: A tectonic-rules based mantle reference frame since 1 billion years ago–implications for supercontinent cycles and plate-mantle system evolution, Solid Earth Discussions, pp. 1–42, 2022.

Munk, W. H. and MacDonald, G. J.: The rotation of the Earth; a geophysical discussion, Cambridge University Press, 1960.

505 Nakagawa, T. and Tackley, P. J.: Lateral variations in CMB heat flux and deep mantle seismic velocity caused by a thermal–chemical-phase boundary layer in 3D spherical convection, Earth and Planetary Science Letters, 271, 348–358, https://doi.org/10.1016/j.epsl.2008.04.013, 2008.

Nakagawa, T. and Tackley, P. J.: Influence of combined primordial layering and recycled MORB on the coupled thermal evolution of Earth's mantle and core, Geochemistry, Geophysics, Geosystems, 15, 619–633, 2014.

510 Olson, P. and Christensen, U. R.: The time-averaged magnetic field in numerical dynamos with non-uniform boundary heat flow, Geophysical Journal International, 151, 809–823, https://doi.org/10.1046/j.1365-246X.2002.01818.x, 2002.

Olson, P., Deguen, R., Hinnov, L. A., and Zhong, S.: Controls on geomagnetic reversals and core evolution by mantle convection in the Phanerozoic, Physics of the Earth and Planetary Interiors, 214, 87–103, https://doi.org/10.1016/j.pepi.2012.10.003, 2013.

Olson, P., Deguen, R., Rudolph, M. L., and Zhong, S.: Core evolution driven by mantle global circulation, Physics of the Earth and Planetary
515 Interiors, 243, 44–55, https://doi.org/10.1016/j.pepi.2015.03.002, 2015.

Olson, P. L., Coe, R. S., Driscoll, P. E., Glatzmaier, G. A., and Roberts, P. H.: Geodynamo reversal frequency and heterogeneous core–mantle boundary heat flow, Physics of the Earth and Planetary Interiors, 180, 66–79, https://doi.org/10.1016/j.pepi.2010.02.010, 2010.

Pais, M. A., Morozova, A. L., and Schaeffer, N.: Variability modes in core flows inverted from geomagnetic field models, Geophysical Journal International, 200, 402–420, https://doi.org/10.1093/gji/ggu403, 2015.

520 Phillips, B. R., Bunge, H.-P., and Schaber, K.: True polar wander in mantle convection models with multiple, mobile continents, Gondwana Research, 15, 288–296, 2009.

Ricard, Y., Fleitout, L., and Froidevaux, C.: Geoid heights and lithospheric stresses for a dynamic Earth, Annales Geophysicae, 2, 267–286, 1984.

Ricard, Y., Spada, G., and Sabadini, R.: Polar wandering of a dynamic Earth, Geophysical Journal International, 113, 284–298,
525 https://doi.org/10.1111/j.1365-246X.1993.tb00888.x, 1993.

Richards, M. A. and Hager, B. H.: Geoid anomalies in a dynamic Earth, J. Geophys. Res., 89, 5987–6002, https://doi.org/10.1029/JB089iB07p05987, 1984.

Ritsema, J. and Lekić, V.: Heterogeneity of seismic wave velocity in Earth's mantle, Annual Review of Earth and Planetary Sciences, 48, 377–401, 2020.

530 Robert, B., Besse, J., Blein, O., Greff-Lefftz, M., Baudin, T., Lopes, F., Meslouh, S., and Belbadaoui, M.: Constraints on the Ediacaran inertial interchange true polar wander hypothesis: A new paleomagnetic study in Morocco (West African Craton), Precambrian Research, 295, 90–116, 2017.

Rost, S., Garnero, E. J., Williams, Q., and Manga, M.: Seismological constraints on a possible plume root at the core-mantle boundary, Nature, 435, 666–669, doi: 10.1038/nature03620, 2005.

535 Schaber, K., Bunge, H.-P., Schuberth, B. S. A., Malservisi, R., and Horbach, A.: Stability of the rotation axis in high-resolution mantle circulation models: Weak polar wander despite strong core heating, Geochem. Geophys. Geosyst., 10, https://doi.org/10.1029/2009GC002541, 2009.

Schaeffer, N.: Efficient spherical harmonic transforms aimed at pseudospectral numerical simulations, Geochemistry, Geophysics, Geosystems, 14, 751–758, 2013.

540 Steinberger, B.: Topography caused by mantle density variations: observation-based estimates and models derived from tomography and lithosphere thickness, Geophysical Journal International, 205, 604–621, https://doi.org/10.1093/gji/ggw040, 2016.

Steinberger, B. and O'Connell, R. J.: Changes of the Earth's rotation axis owing to advection of mantle density heterogeneities, Nature, 387, 169–173, https://doi.org/10.1038/387169a0, 1997.

Su, W.-j. and Dziewonski, A. M.: Simultaneous inversion for 3-D variations in shear and bulk velocity in the mantle, Physics of the Earth
545 and Planetary Interiors, 100, 135–156, 1997.

Tackley, P. J.: Self-consistent generation of tectonic plates in time-dependent, three-dimensional mantle convection simulations 1. Pseudo-plastic yielding, Geochemistry, Geophysics, Geosystems, 1, https://doi.org/https://doi.org/10.1029/2000GC000036, 2000a.

Tackley, P. J.: Self-consistent generation of tectonic plates in time-dependent, three-dimensional mantle convection simulations 2. Strain weakening and asthenosphere, Geochemistry, Geophysics, Geosystems, 1, https://doi.org/https://doi.org/10.1029/2000GC000043, 2000b.

550 Tackley, P. J.: Modelling compressible mantle convection with large viscosity contrasts in a three-dimensional spherical shell using the yin-yang grid, Physics of the Earth and Planetary Interiors, 171, 7–18, https://doi.org/10.1016/j.pepi.2008.08.005, 2008.

Terra-Nova, F., Amit, H., and Choblet, G.: Preferred locations of weak surface field in numerical dynamos with heterogeneous core–mantle boundary heat flux: consequences for the South Atlantic Anomaly, Geophysical Journal International, 217, 1179–1199, 2019.

Trampert, J.: Probabilistic Tomography Maps Chemical Heterogeneities Throughout the Lower Mantle, Science, 306, 853–856, 555 https://doi.org/10.1126/science.1101996, 2004.

Tsai, V. C. and Stevenson, D. J.: Theoretical constraints on true polar wander, J. Geophys. Res., 112, B05 415, https://doi.org/10.1029/2005JB003923, 2007.

Zhang, N. and Zhong, S.: Heat fluxes at the Earth's surface and core–mantle boundary since Pangea formation and their implications for the geomagnetic superchrons, Earth and Planetary Science Letters, 306, 205–216, https://doi.org/10.1016/j.epsl.2011.04.001, 2011.

560 Zhang, S. and Christensen, U.: Some effects of lateral viscosity variations on geoid and surface velocities induced by density anomalies in the mantle, Geophysical Journal International, 114, 531–547, 1993.

Zhong, S., Zhang, N., Li, Z.-X., and Roberts, J. H.: Supercontinent cycles, true polar wander, and very long-wavelength mantle convection, Earth and Planetary Science Letters, 261, 551–564, https://doi.org/10.1016/j.epsl.2007.07.049, 2007.

Zhong, S., McNamara, A., Tan, E., Moresi, L., and Gurnis, M.: A benchmark study on mantle convection in a 3-D spherical shell using 565 CitcomS, Geochemistry, Geophysics, Geosystems, 9, 2008.